DOI: 10.13009/EUCASS2023-503
Aerospace Europe Conference 2023 – 10TH EUCASS – 9TH CEAS

High-fidelity RANS simulations of subsonic and supersonic performance of an Experimental HTB aircraft at 0º, 5º and 10º angles of attack

Daniel Muradás[1], Félix Nieto[1] and Santiago Hernández[1†]
[1]Structural Mechanics Group
University of A Coruña
Campus de Elviña, A Coruña, 15071, Spain
daniel.odriozola@col.udc.es – f.nieto@udc.es – hernandez@udc.es
[†] Corresponding Author

Abstract
The EU has funded the MORE&LESS project aimed at contributing to a more sustainable supersonic aviation. To this end an experimental Hypersonic Test Bed (HTB) vehicle was selected as a case study to conduct high-fidelity CFD simulations. The results obtained adopting steady RANS calculations in the range of Mach numbers (0.4, 2.0) and angles of attack 0º, 5º and 10º are reported. The aerodynamic performance of the aircraft has been addressed evaluating the aerodynamic coefficients in ideal and real flow. Features as the shock wave created at the experimental air-breathing engine and moment coefficient sensitivity to March number have been identified.

1. Introduction

The quest for faster and more sustainable air transport calls for a decide push in supersonic and hypersonic technologies. In Europe, a number of collaborative research projects such as LAPCAT, HEXAFLY or STRATOFLY [1-3] have addressed the conceptual design of vehicles capable of reaching Mach 8 velocities. Japanese companies lead by JAXA have been working on developing a commercial supersonic aircraft by 2030 [4]. Similarly, the USA have joined this competition, and the work by Boom Inc., developing the Overture aircraft, capable of flying at M 1.7, is a good example [5, 6].
One of the recent efforts by the European research community in civil supersonic aviation is the EU Research and Innovation Programme H2020 MORE&LESS (MDO and Regulations for Low-boom and Environmentally Sustainable Supersonic aviation). The consortium is comprised by 5 universities, 6 research centres, 2 large companies, 1 SME and 1 technical association located in the following countries: Italy, USA, France, Germany, Belgium, Spain, Romania, Sweden and the Netherlands.
The work reported here is part of the extensive high-fidelity modelling activities comprised by the project and a completion of previous computational studies [7]. One of the general objectives of the research is to "support the definition of regulations and procedures for the future supersonic aviation through solid technical bases", which comprises "transposing the scientific findings in the fields of aerodynamics, … into guidelines to support the Regulatory Community". Another key objective is "to contribute maintaining world-class knowledge and skills in Europe in the field of supersonic aviation" "by increasing the accuracy of predictive models in the field of aerodynamics".
To reach the aforementioned targets, a prototype of an experimental Hypersonic Test Bed (HTB), provided by the company Reactions Engines, has been selected as study case for the high-fidelity CFD simulations aiming at characterizing the aerodynamic response of the aircraft up to M 5.0.
This paper is organized as follows: the HTB prototype is described and the CFD formulation adopted is introduced along with the main features of the selected computational approach. Afterwards, the finite volume mesh developed for this case is described along with the procedure followed to reach the solution of the steady state turbulent viscous flow around the aircraft. Finally the numerical results obtained at Mach numbers between 0.4 and 2, and at angles of attack (AoA) 0º, +5º and +10º, are reported and analysed to better understand the expected performance of HTB prototype.

DOI: 10.13009/EUCASS2023-503

2. Vehicle description

The preliminary HTB data for the MORE&LESS project features two engines: the first one is an experimental air-breathing engine located in a nacelle on the upper fuselage; and the second one is a rocket engine located at the rear end of the fuselage (see Fig. 1 for a general view depicting the HTB vehicle).
It should be noted that the spike of the experimental engine may be moved aiming at generating an oblique shock-wave intersecting the lip of the cowl; however according to the specification provided, it is fixed between Mach 0 and Mach 2.0, which is the range addressed in this work. During the mission, the experimental nacelle is not operative below Mach 0.575, and up to Mach 1.3 the exhaust flow is expected to experience separation in the bypass burners, and therefore the engine is operating outside the design conditions. Aiming at better modelling this non-optimal operative stage, the area of the experimental nacelle bypass nozzle is adjusted for the different Mach numbers considered in the range (0.6, 1.2).
The HBT is about 24.5 m long and the wingspan is 8.9 m. The prototype includes control surfaces, as canards at the front, which are considered fixed in these preliminary studies. Similarly, the HBT features a V-tail to avoid the interference with the nacelle exhaust.

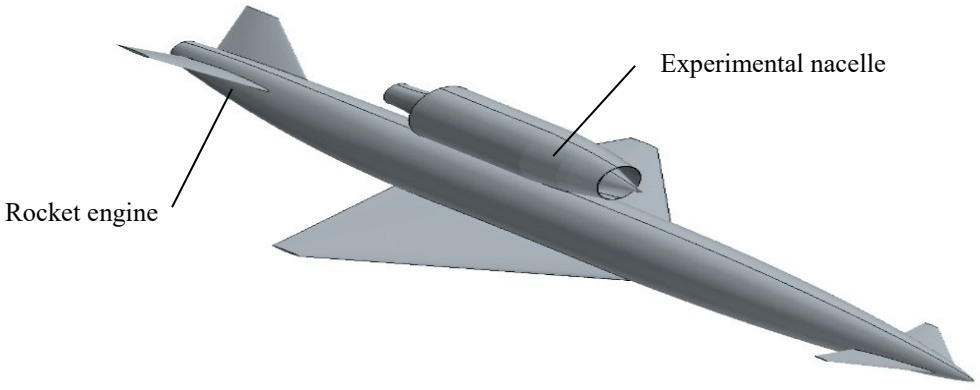

Figure 1: Experimental HTB aircraft geometry

The expected angles of incidence for the ascent phase are between 0º and +5º, while at low speeds the range of considered angles of attack is between -5º and +20º. In the CFD simulations reported herein, angles of attack of 0º, +5º and +10º have been studied at flow speed between Mach 0.4 and Mach 2.0.

3. Formulation

In the next subsections the fundamental formulation for the computational simulations latter reported is introduced.

A. Reynolds averaged Navier Stokes equations

In the numerical simulations whose results are reported next, a steady state compressible viscous flow has been considered along with turbulent effects. Ideal flow conditions have been adopted for the initial flow conditions, while the k-ω turbulence model has been switched on as the simulation progressed. The solver of choice has been Siemens STAR CCM+, whose ability to deal with supersonic flow problems has been well demonstrated in the past [8, 9].
The steady Reynolds Averaged Navier Stokes (RANS) equations are provided in the following:

$$\nabla \cdot (\rho \overline{\mathbf{v}}) = 0, \tag{1}$$

$$\nabla \cdot (\rho \overline{\mathbf{v}} \otimes \overline{\mathbf{v}}) = -\nabla \cdot \overline{p}\mathbf{I} + \nabla \cdot \left(\overline{\mathbf{T}} + \mathbf{T}_{RANS}\right) + \mathbf{f}_b, \tag{2}$$

$$\nabla \cdot \left(\rho \overline{E} \overline{\mathbf{v}}\right) = -\nabla \cdot \overline{p}\overline{\mathbf{v}} + \nabla \cdot \left(\overline{\mathbf{T}} + \mathbf{T}_{RANS}\right)\overline{\mathbf{v}} - \nabla \cdot \overline{\mathbf{q}} + \mathbf{f}_b, \tag{3}$$

where ρ is the fluid density, $\overline{\mathbf{v}}$ is the time-averaged velocity, $\overline{p}$ is the time-averaged pressure and $\overline{E}$ is the time-averaged energy per unit mass. Additionally, $\mathbf{I}$ is the identity Tensor, $\overline{\mathbf{T}}$ is the mean stress tensor, $\mathbf{f}_b$ is the resultant body forces vector and $\overline{\mathbf{q}}$ is the mean heat flux.
The extra term $\mathbf{T}_{RANS}$ represents the stress tensor, that is obtained applying the Boussinesq approximation [10] for the real flow case considered herein:

DOI: 10.13009/EUCASS2023-503

$$\mathbf{T}_{RANS} = 2\mu_t \mathbf{S} - \frac{2}{3}(\mu_t \nabla \cdot \overline{\mathbf{v}})\mathbf{I}, \quad (4)$$

where **S** represents the mean strain rate tensor defined as $\mathbf{S} = 1/2\left(\nabla\overline{\mathbf{v}} + \nabla\overline{\mathbf{v}}^T\right)$.
The turbulent eddy viscosity μ_t is defined as:

$$\mu_t = \rho k T, \quad (5)$$

B. *k-ω* SST turbulence model

In the above equation, k is the turbulence kinetic energy and T is the turbulence dissipation time scale obtained with equation (6). This expression introduces as well the specific dissipation rate ω, which must be solved in the transport equations for the k-ω turbulence model (refer to [11] for the general formulation of the turbulence model).

$$T = \min\left(\frac{\alpha^*}{\omega}, \frac{a_1}{SF_2}\right), \quad (6)$$

In the above equation $S = |\mathbf{S}|$ and F_2 is defined as:

$$F_2 = \tanh\left[\left(\max\left(\frac{2\sqrt{k}}{\beta^*\omega d'}, \frac{500\nu}{d^2\omega}\right)\right)^2\right], \quad (7)$$

Being in Eq. (7) d the distance to the wall and α^*, a_1, C_T and β^* are model coefficients as per table 1.

Table 1: Coefficients in the *k-ω* SST turbulence model.

Coefficient	Value
α_1	0.31 (0.355 for M> 1.6)
α^*	$F_1\alpha_1 + (1 - F_1)\alpha_2$
α_1^* & α_2^*	1
β	$F_1\beta_1 + (1 - F_1)\beta_2$
β_1	0.075
β_2	0.00828
β^*	$F_1\beta_1^* + (1 - F_1)\beta_2^*$
β_1^* & β_2^*	0.09
κ	0.41
σ_k	$F_1\sigma_{k_1} + (1 - F_1)\sigma_{k_2}$
σ_{k_1}	0.85
σ_{k_2}	1
σ_ω	$F_1\sigma_{\omega_1} + (1 - F_1)\sigma_{\omega_2}$
σ_{ω_1}	0.5
σ_{ω_2}	0.856
C_T	0.6

The transport equations in steady state required for the specific turbulent kinetic energy k and the specific dissipation rate ω are the following:

DOI: 10.13009/EUCASS2023-503

$$\nabla \cdot (\rho k \overline{\mathbf{v}}) = \nabla \cdot [(\mu + \sigma_k \mu_t) \nabla k] + P_k - \rho \beta^* f_{\beta^*} (\omega k - \omega_0 k_0) \quad \textbf{(8)}$$

$$\nabla \cdot (\rho \omega \overline{\mathbf{v}}) = \nabla \cdot [(\mu + \sigma_k \mu_t) \nabla \omega] + P_\omega - \rho \beta f_\beta (\omega^2 - \omega_0^2), \quad \textbf{(9)}$$

where μ is the fluid viscosity, k_0 and w_0 are the ambient turbulence values to counteract turbulence decay, σ_k and σ_w are model coefficients whose values were also defined in table 1. Finally, the production terms P_k and P_ω are further explained and synthesized in [12].
The turbulence model also requires the evaluation of the blending function F_1 as:

$$F_1 = \tanh([\min(\Phi_1, \Phi_2)]^4). \quad \textbf{(10)}$$

In the above equation ν is the kinematic viscosity and Φ_1 and Φ_2 are defined as follows:

$$\Phi_1 = \max\left(\frac{\sqrt{k}}{0.09\omega d}, \frac{500\nu}{d^2\omega}\right) \quad \textbf{(11)}$$

$$\Phi_2 = \frac{2k}{d^2 CD_{k\omega}} \quad \textbf{(12)}$$

$$CD_{k_\omega} = \max\left(\frac{1}{\omega}\nabla k \cdot \nabla, 10^{-20}\right) \quad \textbf{(13)}$$

C. Aerodynamic coefficients

The preliminary assessment of the aerodynamic performance of the HTB vehicle is based upon the computation of the aerodynamic coefficients that will be validated with wind tunnel data at a latter stage of the MORE&LESS project. These non-dimensional coefficients are defined as:

$$C_L = \frac{L}{\frac{1}{2}\rho U^2 S}, \quad C_D = \frac{D}{\frac{1}{2}\rho U^2 S} \quad \text{and} \quad C_M = \frac{M}{\frac{1}{2}\rho U^2 S c}. \quad \textbf{(14)}$$

In the former equations, L, D and M are the lift and drag forces and pitching moment, respectively while ρ and U are the density and velocity of the freestream, respectively. Lastly, S is the surface area of the aircraft wind and c is the wing chord. It is to note that the aerodynamic forces comprise bot the airframe and the experimental nacelle contribution.

4. Finite volumes mesh and boundary conditions

A. Flow domain and mesh discretization

Aiming at reducing the cells count in the finite volume mesh, the symmetry properties of the HTB vehicle and the studied cases that do not account for sideslip effects are considered to define a flow domain that models the right half of the aircraft and the surrounding flow. The external flow domain is cone-shaped to further reduce the required number of elements. As the focus of the study is set upon the aerodynamics of the aircraft, the downstream extensions of the domain is moderate. In Fig. 2, a general views of the fluid domain comprising the geometry of the HTB are depicted.
The finite volume mesh has been defined using the meshing the capabilities in STAR CCM+, adopting the proprietary polyhedral type elements, which enable the subdivisions in the flow domain for applying automatic mesh refinement tools. The base size element adopted for the spatial discretization is the 4% of the airframe length, taken here as reference dimension. As the mesh is further refined in the regions of interest, such as wing, canard, V-tail or nacelle inlet, the size of the elements reach 0.04% of the reference length. Further mesh refinement is introduced in the boundary layer mesh of prismatic elements around the solid surfaces of the aircraft, imposing a maximum non-dimensional height for the first layer $y^+ \leq 1$. In this manner, a low Reynolds wall modelling approach is adopted, aiming at obtaining a more accurate representation of flow features such as separation and eventually reattachment, remarkably at higher angles of attack.
In Fig. 3, a general view of the mesh around the HTB aircraft is provided, where the high-density mesh regions can be identified along with the symmetry plane. In Fig. 4, detailed images depicting the high density mesh in the vicinity of the experimental nacelle are reported. It is to note in the last figure, the boundary layer mesh defined for the spike and the cowl.

DOI: 10.13009/EUCASS2023-503

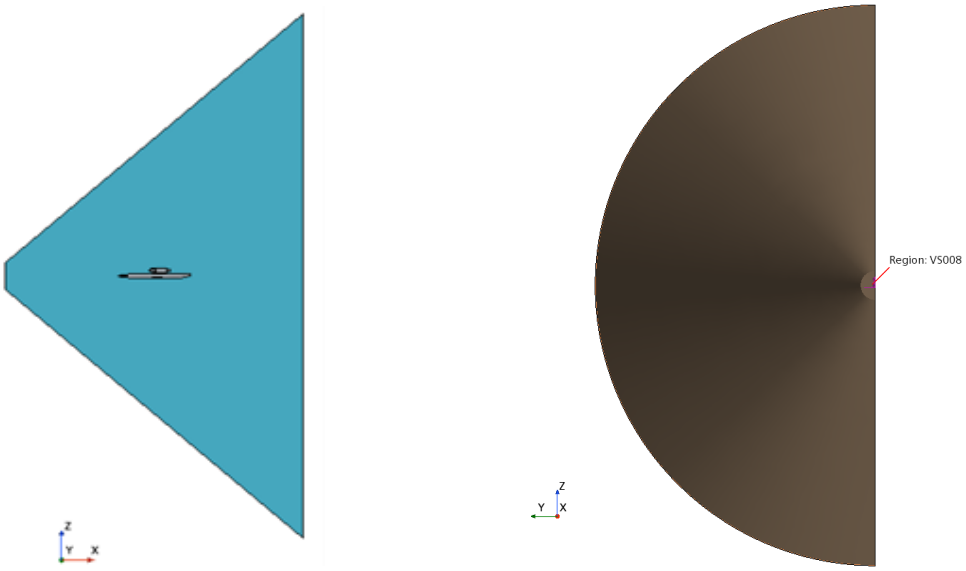

a) Side view b) Front view

Figure 2: General cone-shaped flow domain comprising the HTB vehicle.

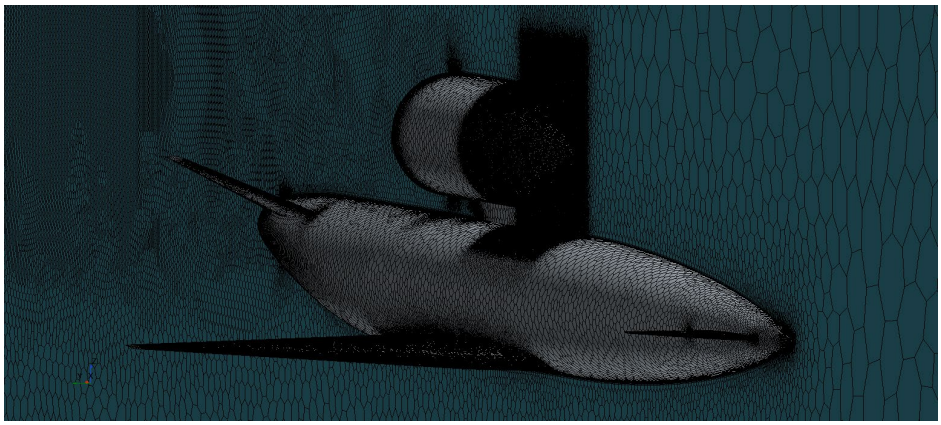

Figure 3: General mesh definition (aircraft and symmetry plane 3D view).

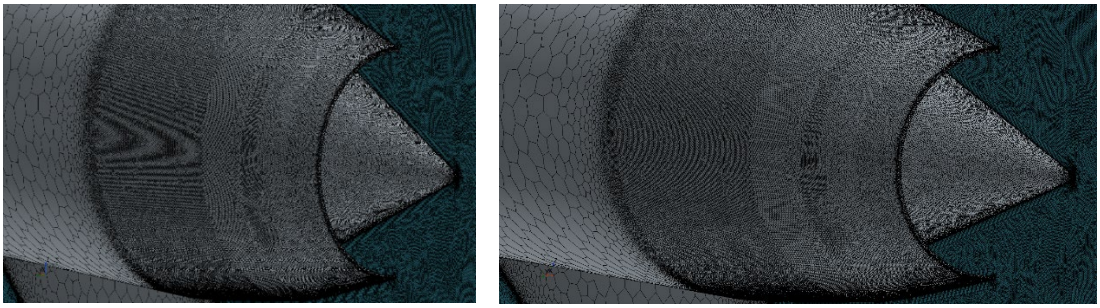

a) Detail at the experimental nacelle. b) Detail around the scowl and the spike

Figure 4: Detail view of the high-density boundary layer mesh surrounding the experimental nacelle.

DOI: 10.13009/EUCASS2023-503

B. Boundary conditions

In an external aerodynamics problem, as the one introduced herein, freestream inlet conditions must be defined, along with the outlet boundary later downstream. Also, the aircraft surfaces must be defined as solid walls comprising the no penetration and no slip conditions for a viscous fluid model. In this case, the analysis of the effects produced by the experimental engine on top of the airframe and the rocket engine has been considered of interest. Henceforth, the intake at the nacelle, along with the exhaust flow at the nacelle bypass and core nozzles, and the rocket engine nozzle should be considered in the high-fidelity CFD model.

The definition of the right values for the nacelle intake, which is modelled as an outlet, encloses some difficulties. To satisfy the mass conservation principle, the nacelle must exhaust the same quantity of air as it breathes, so the average intake pressure must be specified, but at the current design stage, this condition is not properly assessed. Some 2D and 3D simulations of the isolated nacelle were carried out setting an iterative approach that would vary the intake pressure of the inlet until the intake and exhaust mass flow match. The proposed method provided good estimates for subsonic and transonic cases, while for the supersonic cases, as stable pressure convergence was not achieved, some minor discrepancies in the mass balance were allowed as its impact in the aerodynamics of the aircraft is minimal.

The exhaust conditions at the nozzle outlets are modelled as supersonic outlets at constant Mach number (named as stagnation inlets in STAR CCM+), where the temperature and pressure difference with the freestream flow are known. The supersonic static pressure and the total temperature can be obtained using the isentropic expressions in the following equations:

$$\frac{p_s}{p_t} = \left(1 + \frac{\gamma - 1}{2} M^2\right)^{-\frac{\gamma}{\gamma - 1}}, \tag{15}$$

$$\frac{T}{T_t} = \left(1 + \frac{\gamma - 1}{2} M^2\right)^{-1}. \tag{16}$$

In the former equations, p_s and p_t are the supersonic static pressure and total pressure, respectively; while T is temperature and T_t the total temperature. Furthermore, γ is the specific gas constant ratio for air, and M is the Mach number.

Lastly, as the rocket is powered by the combustion of hydrogen and oxygen, the mass fraction of water and hydrogen, namely the percentage of each gas, must be specified for the rocket outlet. The output of the nacelle core and bypass will be assumed to be exclusively air, as the effects of fuel are considered negligible.

The nacelle bypass outlet may experience internal flow separation at subsonic regimes, as the design mass flow cannot be exhausted by the engine. Given the Mach speed, pressure and temperature at the nacelle bypass nozzle, the mass flow can be computed as:

$$\dot{m} = pAM\sqrt{\frac{\gamma}{RT}} \tag{17}$$

In Eq. (17) $\dot{m}$ stands for the mass flow, A for the area, while γ and R are the specific gas constant ratio and the molar gas constant. The nacelle bypass outlet area was reduced until its mass flow output matched the data provided using the previously stated equation.

5. Finite volumes mesh and boundary conditions

The relatively extreme values for the velocity, pressure and temperature gradients at supersonic regimes for the HTB vehicle pose a challenge for the CFD solver. Consequently, a sequential resolution process has been developed, at the main steps are summarized in Fig. 5. Each simulation is started assuming ideal flow and a relatively coarse mesh downstream the nozzles. Progressively, the mesh is refined and real flow properties are introduced. The procedure also serves as a mesh refinement sensitivity assessment.

DOI: 10.13009/EUCASS2023-503

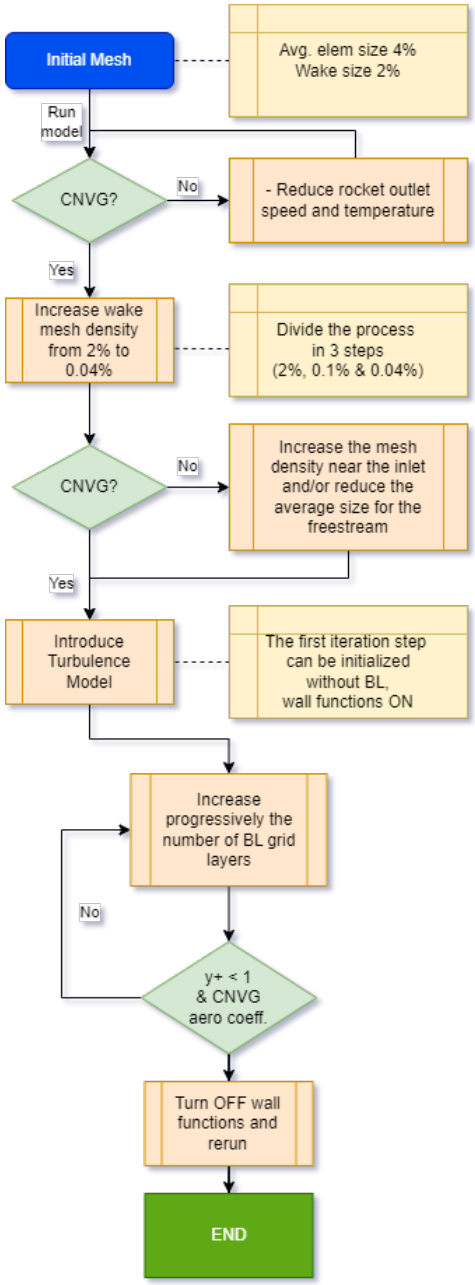

Figure 5: Flow chart for the solution procedure (CNVG stands for convergence).

The main stages in the process to reach the steady solution considering real fluid properties and turbulence are summarized next:

1) *Ideal inviscid flow initialization*. All the cells in the fluid domain are assigned free stream properties at the initial conditions, while for the nacelle and rocket exhausts the flow is set at Mach 3.45. The cells located in the wake of the nozzles are sized as 2% of the airframe length and no boundary layer is considered attached to the solid surfaces.
2) *Remeshing in the wake of the nozzles*. As the simulation progresses reaching the prescribed residual targets, the mesh is refined, particularly in the wake of the nozzles from 2% to 0.4% of the reference airframe length. Other boundary conditions, such as outlet speed and temperature, are adjusted as required for each case. An example of the differences in the Mach number field at different stages is provided in Fig. 6.
3) *Real turbulent flow*. Once the ideal flow solution has reached the desired residuals for the variables of interest and the general grid density is satisfactory, real turbulent flow properties are introduced. At this stage, the boundary layer mesh attached to the solid surfaces is introduced and is progressively refined until the maximum $y^+ \leq 1$ condition is met. The boundary layer has been defined with 22 layers, although in some

DOI: 10.13009/EUCASS2023-503

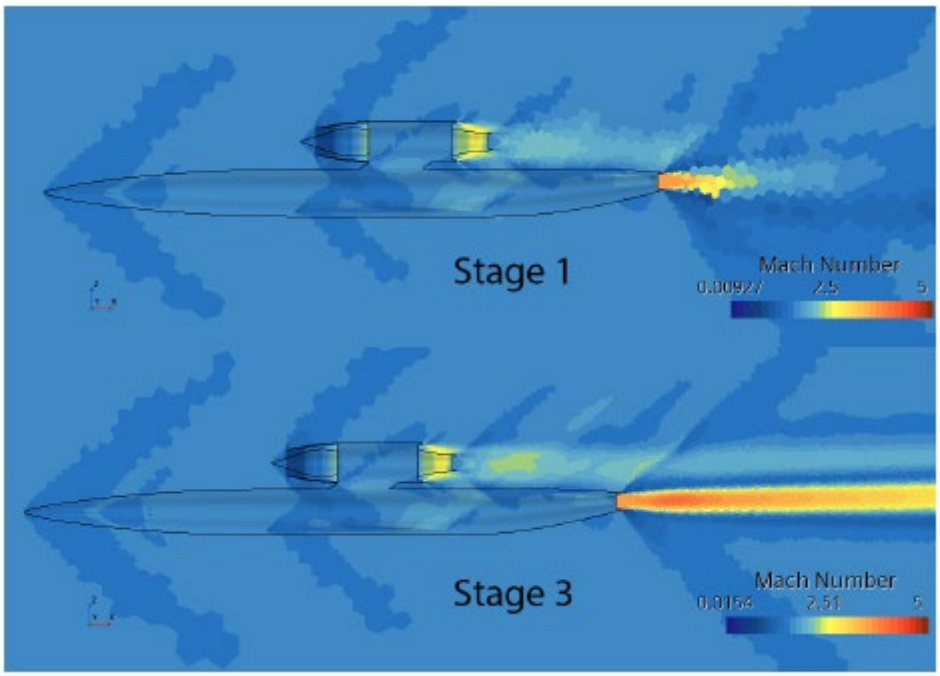

Figure 6: Mach number fields at the symmetry plane in stages 1 and 3, considering ideal flow (Mach 1.6; AoA= 6º).

In Fig. 7, the iteration history along the process previously described for the drag coefficient of case Mach 2.0 and AoA=0º is provided. It can be noted the effect of mesh refinement for the ideal flow at the initial stages, as well as the introduction of real turbulent flow properties. In the final stages, as the boundary layer mesh is refined the impact in the drag coefficient value is minimal.

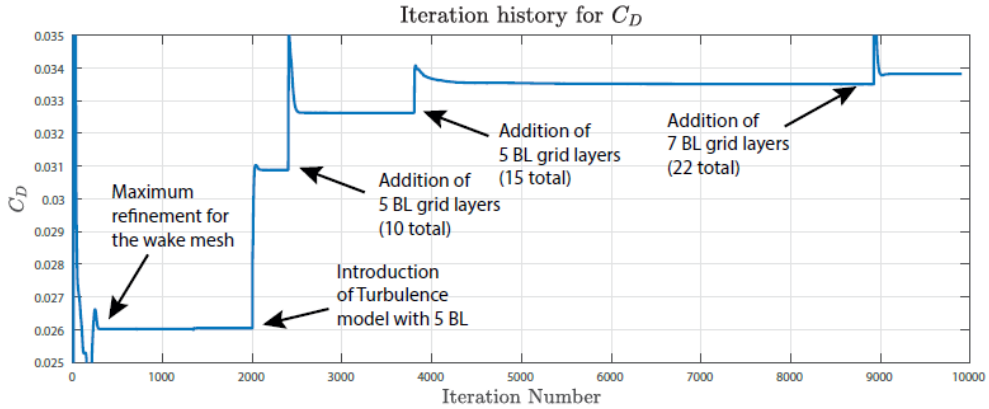

Figure 7: Drag coefficient iteration history (Mach 2.0; AoA= 0º).

6. Numerical results

In this section, the aerodynamic characterization of the HTB aircraft based on the steady compressible real flow simulations conducted for AoA 0º, 5º and 10º and 0º sideslip is reported. It is to note that cruising conditions have been considered and the basic position for the control surfaces is adopted as this work aims at providing only a preliminary assessment of the experimental HTB vehicle. The results comprise the aerodynamic coefficients considering ideal and real flow, the steady state pressure coefficient distributions over the vehicle surfaces and a more detailed study of pressure coefficients over three sections of the wing.

A. Aerodynamic coefficients

The aerodynamic coefficients are evaluated according to Eq. (14). In tables 2 and 3, these results are reported for 0º and 5º AoA, considering ideal and real turbulent flow for a selection of Mach values, covering subsonic and supersonic

DOI: 10.13009/EUCASS2023-503

conditions. It is to note that the differences in the values obtained for ideal or real flow are relatively small for lift and moment, but are more significant for the drag coefficient.

Table 2: Aerodynamic coefficients AoA 0º

	Ideal flow			Real flow		
Mach	C_L	C_D	C_M	C_L	C_D	C_M
0.4	0.0128	0.1279	0.2347	0.0121	0.1421	0.2393
0.6	0.0088	0.0735	0.1149	0.0076	0.0894	0.126
0.8	0.0111	0.0461	0.0209	0.0099	0.059	0.0269
0.95	0.0215	0.0484	-0.0556	0.0153	0.0588	-0.0325
1.05	0.0122	0.0603	-0.0265	0.0094	0.0711	-0.0237
1.2	-0.0103	0.0527	0.0633	-0.0113	0.0626	0.0765
1.6	-0.0592	0.0356	0.239	-0.05694	0.0451	0.2237
2.0	-0.0379	0.0266	0.1925	-0.0396	0.0338	0.2006

Table 3: Aerodynamic coefficients AoA 5º

	Ideal flow			Real flow		
Mach	C_L	C_D	C_M	C_L	C_D	C_M
0.95	0.2752	0.0759	-0.1393	0.2633	0.0797	-0.1138
1.05	0.1866	0.0961	-0.1389	0.1801	0.1053	-0.1103
1.2	0.2309	0.0760	-0.0982	0.2268	0.0796	-0.0793
1.6	0.1631	0.0467	-0.0745	0.1618	0.0556	0.0690
2.0	0.1640	0.0387	-0.0173	0.1591	0.0470	-0.0016

The results reported in the tables above for AoA 0º and 5º, show a general trend related with the decrement in the lift and drag coefficients as the Mach number increases. A detailed review of the values obtained for the drag coefficient shows a slight increment at Mach 1.0 and a clear decrease for higher Mach numbers as the flow density diminishes at supersonic regime. For a sound interpretation of the changes in the lift coefficient, a detailed study of the pressure coefficient distributions over the entire aircraft is required and this is addressed in the following subsection. The analysis of the moment coefficient at different Mach numbers show certain variability as the moment is certainly sensitive to the value of the resultant lift force and its sign. It is to note that this is a preliminary assessment of aerodynamic performance, hence trimming of the control surfaces is not considered.
In table 5, the numerical results considering real flow obtained for AoA 10º are reported for three different values of Mach number. It is remarkable the large sensitivity in the moment coefficient as the Mach number is close to 1.

Table 4: Aerodynamic coefficients AoA 10º

	Real flow		
Mach	C_L	C_D	C_M
0.4	0.4652	0.1996	0.1716
0.95	0.56752	0.1533	-0.2614
1.2	0.4863	0.1408	-0.2318

DOI: 10.13009/EUCASS2023-503

B. Pressure coefficient distributions over the airframe and Mach flow fields

The resultant aerodynamic forces and moment acting on the aircraft are due to the pressure distribution and viscous stresses acting on the solid surfaces. In figure 8a, the pressure coefficient distribution over the upper fuselage is presented for Aoa 0º and Mach 2. It is to note the localized increment in the pressure acting on the upper side of the wings (yellow color in the referred figure). This is due to the shock wave caused by the nacelle located on top of the airframe. This feature if further assessed in Fig. 8b, where the isosurfaces of the pressure coefficient flow fields are provided. This increase in the pressure action on the upper side of the wing at supersonic velocity is responsible for the decrease in lift coefficient as the Mach number increases, and the subsequent impact in the moment coefficient, mentioned in the previous subsection. In Fig. 9, equivalent graphical information is provided for the Mach 1.2 AoA 10º case.

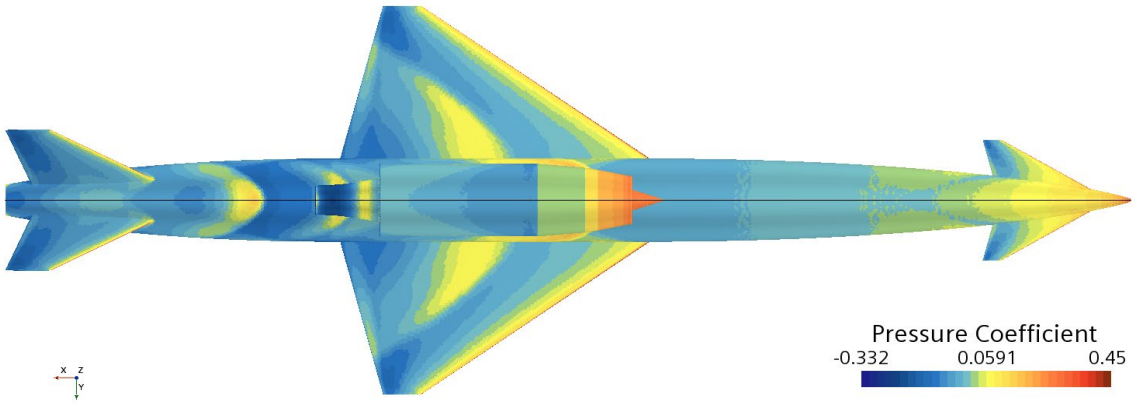

a) C_p distribution on the HTB vehicle (Top view).

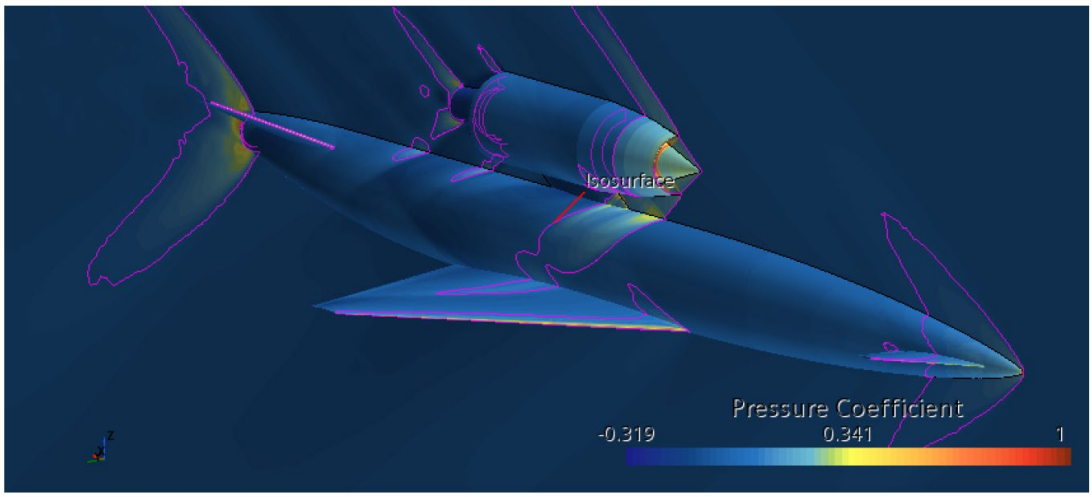

b) C_p isosurface for the flow around the HTB vehicle (3D view including symmetry plane).

Figure 8: Pressure coefficient distribution (Mach 2.0; AoA= 0º).

DOI: 10.13009/EUCASS2023-503

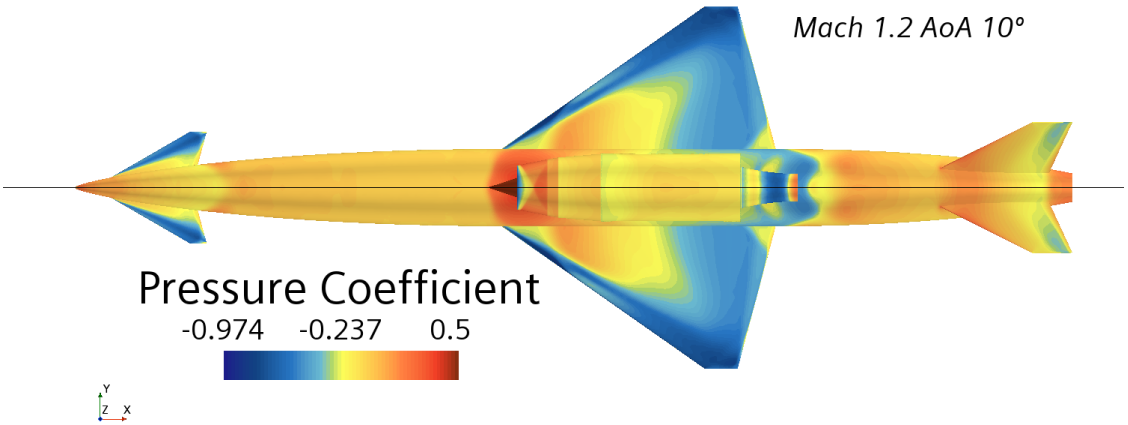

a) C_p distribution on the HTB vehicle (Top view).

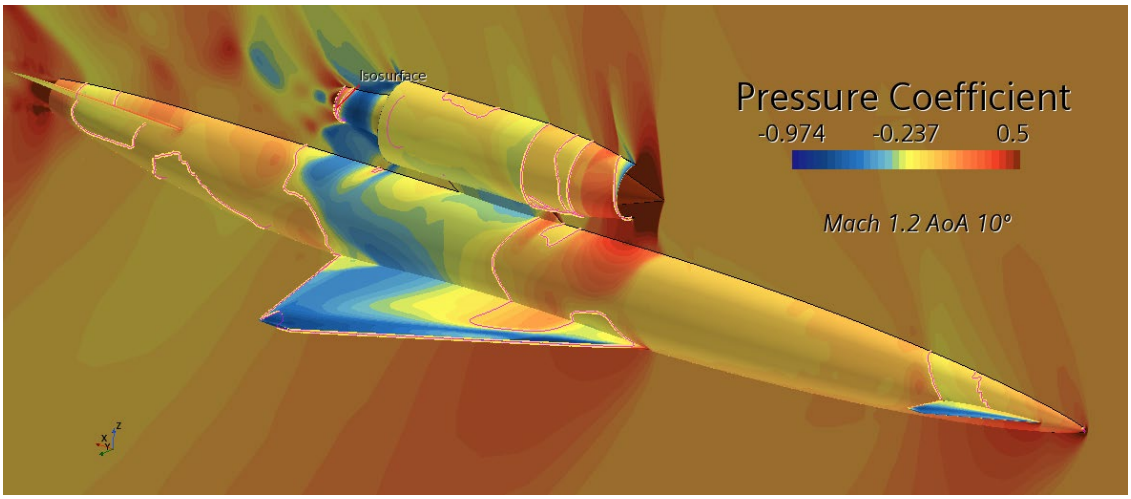

b) C_p isosurface for the flow around the HTB vehicle (3D view including symmetry plane)

Figure 9: Pressure coefficient distribution (Mach 1.2; AoA= 10º).

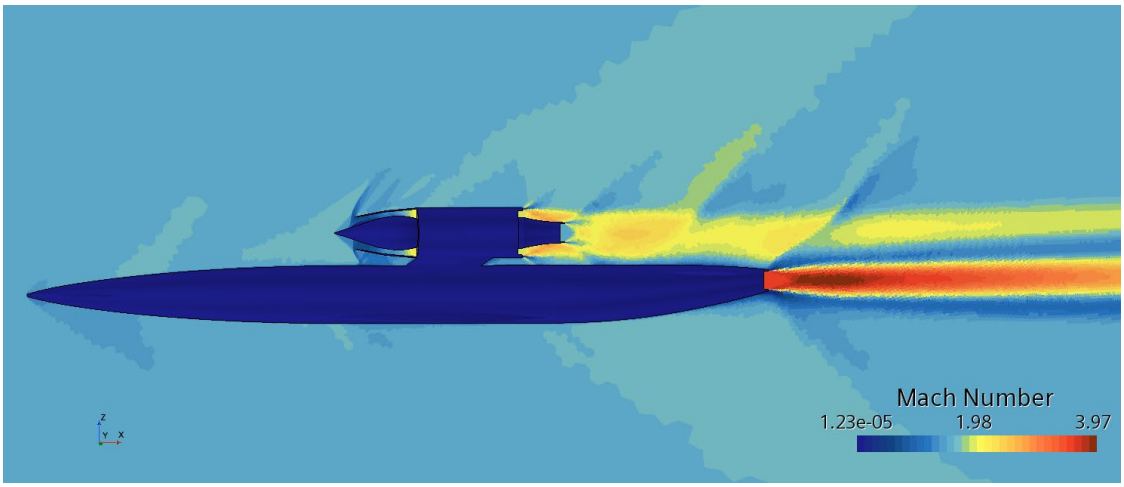

a) Mach 1.6, AoA=5º

Figure 10: Mach number field over the symmetry plane

DOI: 10.13009/EUCASS2023-503

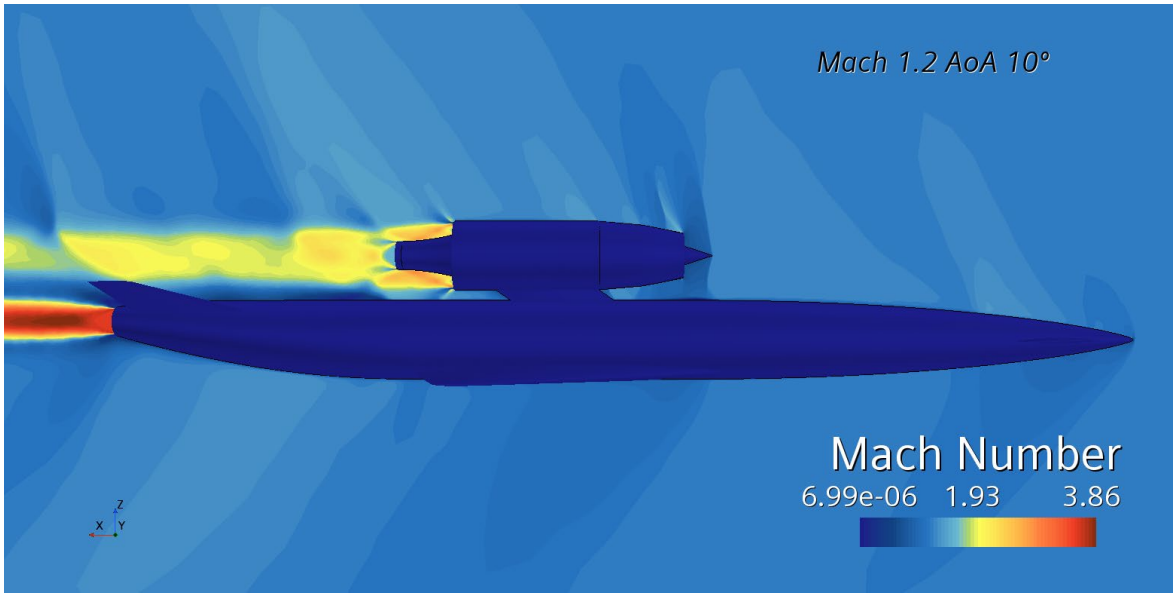

b) Mach 1.2, AoA=10º

Figure 10: Mach number field over the symmetry plane (cont´d)

The numerical studies have enabled the identification of further interference effects of the supersonic jets with the V-tail of the aircraft, as well as among the nacelle and rocket outlets. In Fig. 10, the Mach number field over the symmetry plane is depicted for cases Mach 1.6 and AoA 5º, as well as Mach 1.2 and AoA 10º. Discontinuities in the supersonic exhaust of the nacelle can be identified at the position of the V-tail leading edge and just downstream the rocket outlet. The numerical simulations conducted in the frame of this preliminary study have allowed the identification of certain design issues that would require further study as the design process advances.

C. Pressure coefficient distributions over the wings

Evidently, the aerodynamic performance of the aircraft is mainly dictated by the flow features at the wings. Aiming at more precisely understand the phenomena taking place for different Mach numbers and angles of attack, in figure 11, the pressure coefficient profiles at three sections along the wingspan, named Tip, Mid and Root sections, are reported. In agreement with the C_p fields in figure 8, the root and mid sections show a “hump” of positive pressure on the upper side of the wing caused by the shock wave created by the nacelle. In fact, it is noted that this “hump” diminishes and moves downstream as the Mach number increases.

In figure 12, the equivalent information is provided for the AoA 5º case at Mach numbers 1.6 and 2.0. In the charts, for the Root and Mid sections, the “hump” in the pressure coefficient can still be identified, although it is not as abrupt as for the Mach 2.0 AoA 0º case.

DOI: 10.13009/EUCASS2023-503

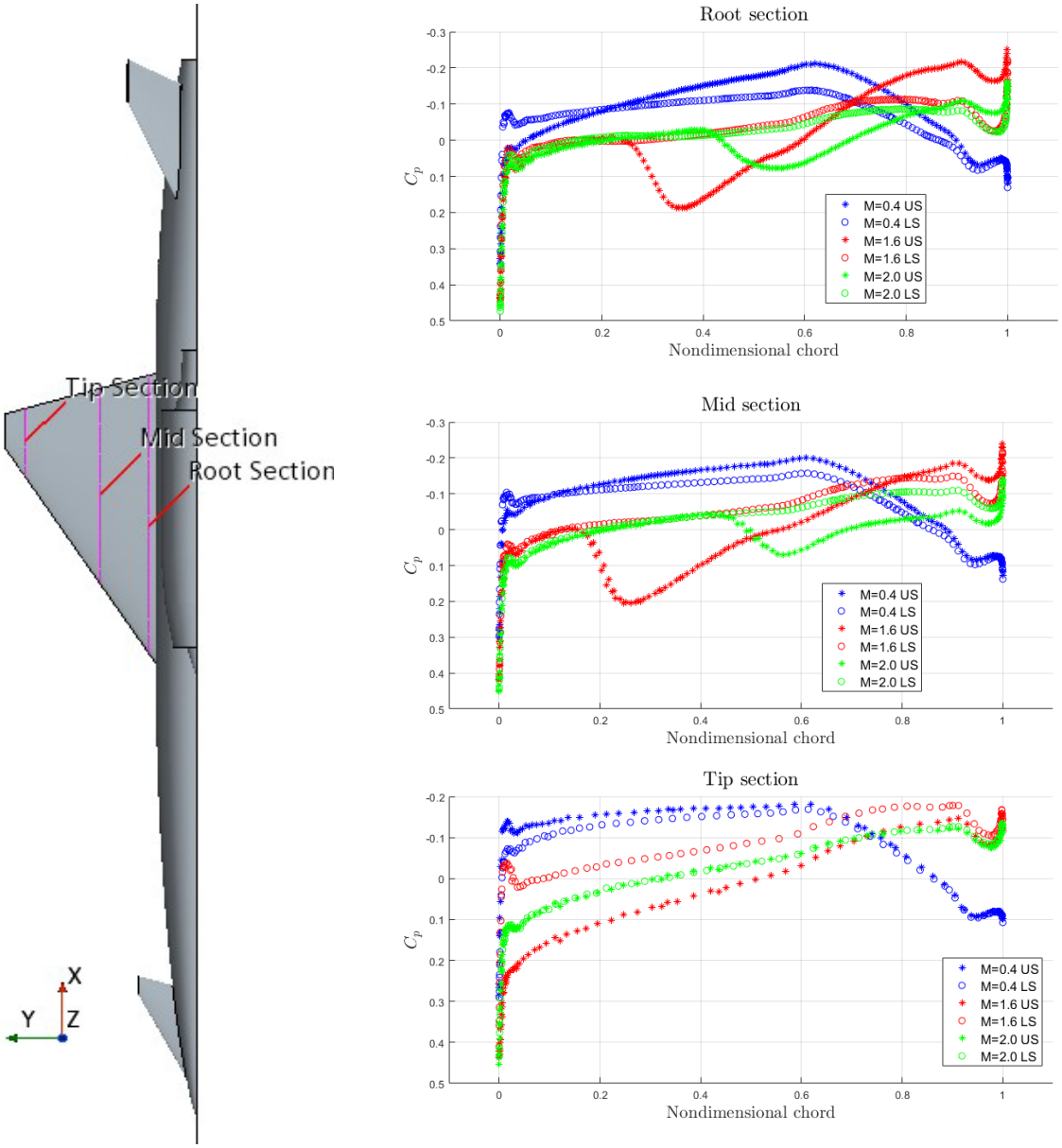

Figure 11: Pressure coefficient profiles at Root, Mid and Tip section (AoA= 0º).

DOI: 10.13009/EUCASS2023-503

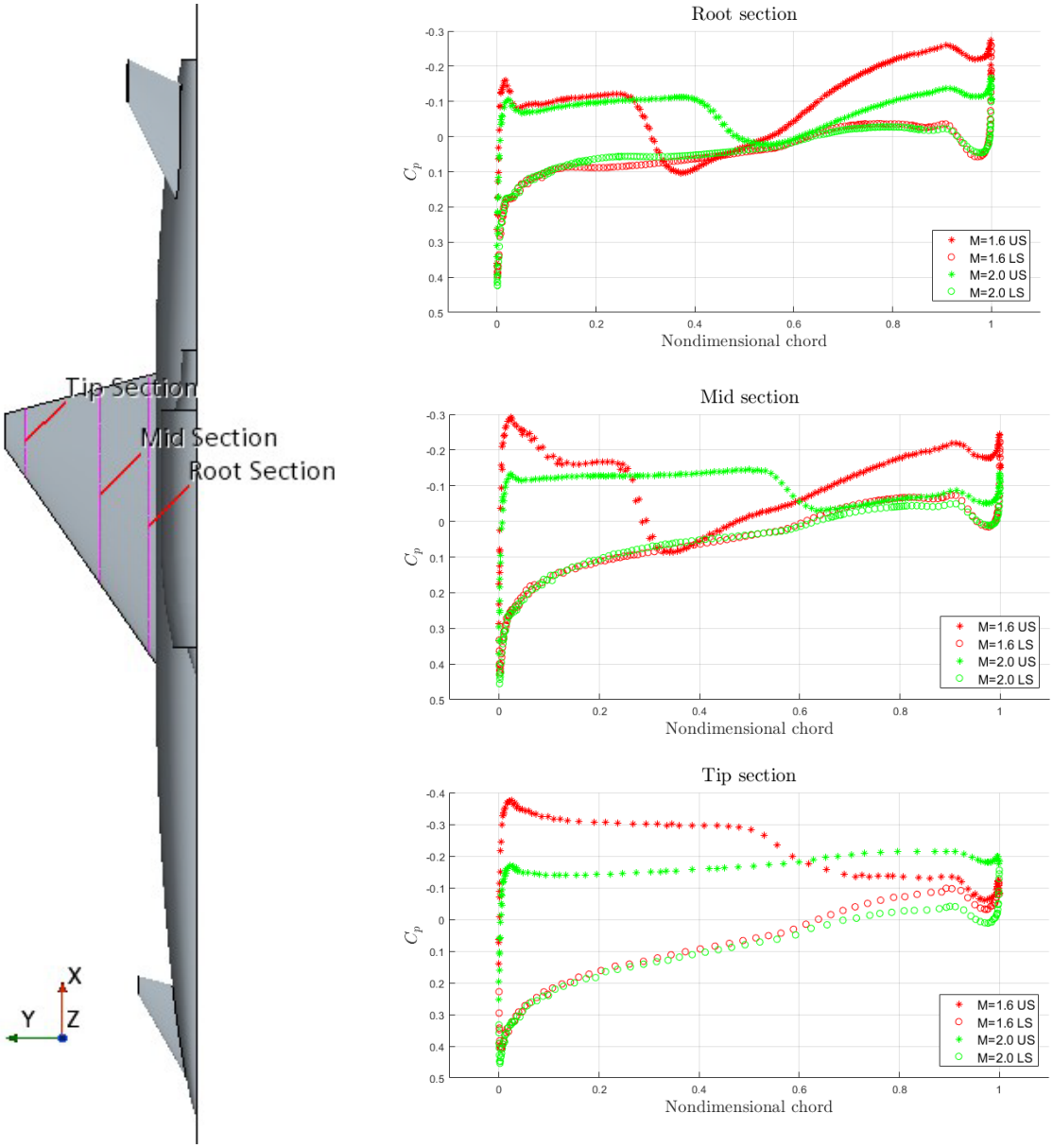

Figure 12: Pressure coefficient profiles at Root, Mid and Tip section (AoA= 5º).

7. Conclusions

This work reports the RANS simulations conducted for an experimental HTB aircraft at 0º sideslip, Mach number in the range (0.4, 2.0) and angles of attack of 0º, 5º and 10º. One of the main challenges in the study is the initialization of the flow. To this end, ideal flow is adopted for the initial iteration stages and the mesh is subsequently refined, until real turbulent flow is considered and a fine boundary layer mesh is introduced satisfying the requirements of the low Reynolds wall modeling approach ($y^+ \leq 1$).

Using CFD simulations, the cruising conditions at 0º AoA have been studied considering a large number of Mach numbers up to 2.0, hence considering both subsonic and supersonic regimes. Some interesting features have been identified, such as the shock wave generated by the air-breathing engine mounted on the upper fuselage that impacts the pressure distribution on the upper side of the wings. Similarly, the nacelle outlet jet interferes slightly with the V-tail and with the rocket engine exhaust. For AoA 5º and 10º, only a limited number of Mach numbers have been studied. Qualitatively, the aerodynamic response is similar to the AoA 0º case, although the aerodynamic coefficients are higher and the sensitivity of the moment coefficient with the Mach number is remarked.

DOI: 10.13009/EUCASS2023-503

The numerical simulations conducted in the frame of this preliminary study have allowed the identification of certain design issues that would require further study as the design process further advances. It should be borne in mind that this HTB case is a preliminary design to be further refined as the design process advances.
The MORE&LESS project will still go ahead for quite some time, addressing a variety of topics related with a more sustainable future supersonic aviation. From an aerodynamics perspective, the comparison of the numerical results reported herein with the outcome of planned wind tunnel tests would represent a milestone for the assessment of the accuracy that can be expected from high-fidelity RANS simulations.

Acknowledgments

This piece of research conducted in the frame of the MORE&LESS project, has been funded by the EU Horizon 2020 Research and Innovation Programme, under Grant Agreement GA-101006856. Professors Hernández and Nieto acknowledge the funding received from the Galician Regional Government through the research grant reference ED131C 2021/33.
The numerical simulations have been completed in the Finisterrae III cluster at the Galician Supercomputing Centre (CESGA).

References

[1] Steelant, J., and Langener, T. September 2014. “The LAPCAT-MR2 hypersonic cruiser concept”, in 29th Congress of the International Council of the Aeronautical Sciences.
[2] Steelant, J., Langener, T., Hannemann, K., Marini, M., Serre, L., Bouchez, M. and Falepim, F. 2015. Conceptual Design of the High-Speed Propelled Experimental Flight Test Vehicle HEXAFLY.
[3] April 2018. “Stratospheric flying opportunities of high-speed propulsion concepts” in Topic MG-1-14-2016-2017 – Breakthrough innovation STARTOFLY. European Commission Horizon 2020.
[4] Finlay, M. June 2021. “Japan expects to develop supersonic planes by 2030” Simply Flying.
[5] Trimble, S. November 2017. “Boom supersonic to pick engines in 2018”, Flight Global.
[6] Norris, G. July 2022. “Boom unveils new look Overture and Northrop common partnership”, Flight Global.
[7] Muradás, D., Nieto, F. and Hernández, S. 2023. “CFD Simulations of an Experimental Hypersonic Test Bed Aircraft in Subsonic and Supersonic Regime. 2023 IEEE Aerospace Conference.
[8] Wang, T., Wang H. and Tang, G. October 2016. “Benchmarking the STAR CCM+ compressible flow solver by simulating typical compressible flow problems: A case study and comparison”, in Theory, Methodology, Tools and Applications for Modelling and Simulation of Complex Systems. Singapore. Springer Singapore, pp. 379-391.
[9] Hanke, J. and Krcmar, M. 2020 Forum. Adaptative Mesh Refinement of Hypersonic Shock and Wake Structures in Simcenter STAR CCM+. AIAA Aviation.
[10] Wilcox, D.C. “Turbulence Modeling for CFD”, DCW Industries, 3rd Edition.
[11] Accessed 8 October 2022. Langley Research Center Turbulence Modeling Resource. “The Menter Shear Stress Transport Turbulence Model”. https://turbmodels.larc.nasa.gov/sst.html.
[12] Siemens Digital Industries Software, “Simcenter STAR CCM+ User Guide, version 2021.1, in k-omega Model., pp. 7784-7789.